Journal of Integrated
SCIENCE & TECHNOLOGY

Efficient synthesis of $Zn_{1-x}Yb_xO$ nanoparticles at low temperatures for photocatalytic application

Trinh Duc Thien[1], Hoang Van Thanh[2], Le T.M. Cham[1], Pham Duc Thang[3], Nguyen Dang Co[4], Nguyen Van Thang[4], Nguyen Duc Chung[4], Tran Quang Vinh[4], Le T.T. Linh[4], Nguyen Dinh Lam[4,*]

[1]Faculty of Physics, Hanoi National University of Education, 136 Xuan Thuy Road, Cau Giay District, Hanoi, 11310, Vietnam. [2]Phenikaa University Nano Institute (PHENA), PHENIKAA University, Hanoi 12116, Vietnam. [3]Faculty of Physics, VNU University of Science, Vietnam National University, Hanoi, 334 Nguyen Trai, Thanh Xuan district, Hanoi, 11416, Viet Nam. [4]Faculty of Engineering Physics and Nanotechnology, VNU-University of Engineering and Technology, 144 Xuan Thuy Road, Cau Giay District, Hanoi, 11310, Vietnam

Submitted on: 12-Sep-2024, Accepted and Published on: 02-May-2025

Article

ABSTRACT A simple low-temperature assisted co-precipitation approach produced $Zn_{1-x}Yb_xO$ nanoparticles. The manufactured samples have a hexagonal wurtzite structure, according to XRD. Yb doping increased average crystal diameter and microstrain. UV-Vis spectroscopy revealed minimal optical band gap changes, with a characteristic ZnO absorption edge at 378 nm and a Yb photosensitive center's $^2F_{7/2}$ - $^2F_{5/2}$ 2 transition peak at 980 nm. Ferromagnetic properties emerged when Yb impurities exceeded 5%. Photocatalytic studies showed that 50 mg of Zn1-xYbxO nanoparticles effectively decomposed 10 mg/L rhodamine B (RhB) under a 250W mercury lamp within 30 minutes. $Zn_{1-x}Yb_xO$ nanoparticles catalytic activity relies on Yb content. The sample with 5% $Zn_{0.95}Yb_{0.05}O$ had the highest photocatalytic performance.

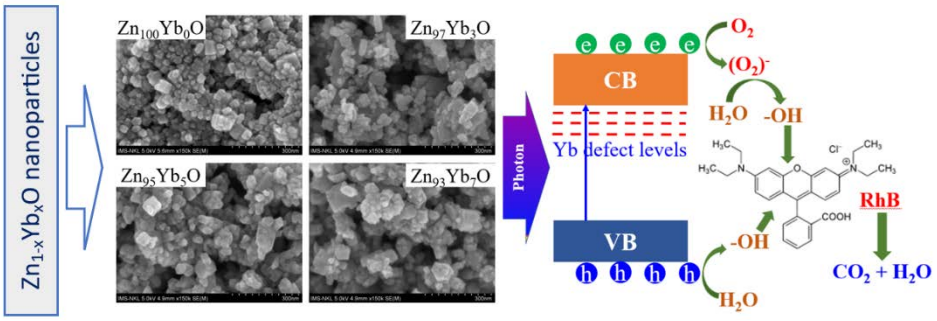

Keywords: Efficient low temperature synthesis, nanoparticles, Yb doping, photocatalysis, wurtzite structure.

INTRODUCTION

In the present century, notable progress has been achieved in the field of nanotechnology, particularly in the creation of novel functional nanomaterials that possess improved characteristics.[1] The progress can be attributed primarily to the substantial surface area of nanoparticles, which facilitates the production of reactive oxygen species. Nanoparticles exhibit a high surface area-to-volume ratio, which greatly enhances their efficacy as catalysts.[2] Zinc oxide (ZnO) nanoparticles become highly valuable in nanotechnology, as they offer enhanced functionalities to materials when compared to their larger counterparts. ZnO applications encompass water and air disinfection, photocatalytic oxidation of diverse pollutants, such as pesticides and dyes, and their utilization as drug carriers. The efficiency of nanoparticles in photocatalysis is closely linked to their surface area. It is crucial to have a large surface area and small crystallite size to induce oxygen defects. and increase the production of reactive oxygen species. Hence, they are increasingly utilized in the domains of optics, biomedicine, electronics, and photocatalysis.[3–9]

Current studies focus on investigating the photocatalytic abilities of modified and improved ZnO nanoparticles. ZnO nanocrystals have the capacity to effectively degrade organic contaminants by photocatalysis.[8,9] Significantly, ZnO nanoparticles that were altered with silver showed exceptional photocatalytic efficacy.[10,11] These nanoparticles are very important for protecting the environment due to their cost-effectiveness, lack of toxicity, chemical stability, and outstanding photocatalytic capability. Moreover, their ability to efficiently absorb ultraviolet (UV) radiation makes them superior than titanium dioxide (TiO_2).[12]

The nanoparticle synthesis method is crucial in attaining the desired quality through precise control of the shape and size. Chemical methods provide superior manipulation of particle size

*Corresponding Author: Nguyen Dinh Lam
Email: lamnd2005@vnu.edu.vn

Cite as: *J. Integr. Sci. Technol., 2025, 13(6), 1132.*
URN:NBN:sciencein.jist.2025.v13.1132
DOI:10.62110/sciencein.jist.2025.v13.1132

and morphology. Incorporating appropriate elements, such as Al, Pt, Au, and rare earth (RE) elements, into ZnO nanoparticles improves their surface characteristics, as well as their optical and electrical properties, resulting in an enhancement of their photocatalytic activity.[13–20] Rare earth (RE) elements, with their distinctive 4f orbital configuration, effectively capture electrons, resulting in a decrease in the rate of electron/hole recombination and the formation of impurity energy levels within the ZnO bandgap resulting in enlarger the optical absorption range.[4,13,20]

In this study, the $Zn_{1-x}Yb_xO$ nanoparticles were synthesized using a low-temperature assisted co-precipitation method. The aim was to achieve high nanoparticle production efficiency at a low cost while maintaining high quality of nanoparticles. An extensive analysis was conducted on $Zn_{1-x}Yb_xO$ nanoparticles to examine their structure, surface morphology, optical properties, and photocatalytic capability.

EXPERIMENT

$Zn_{1-x}Yb_xO$ nanoparticles (x = 0.00 to 0.07) were synthesized by temperature-assisted coprecipitation. The synthesis employed $Zn(CH_3COO)_2.2H_2O$ (>99%), $YbCl_3.6H_2O$ (99.9%), KOH, and DI water as initial reagents. To begin with, $Zn(CH_3COO)_2.2H_2O$ and $YbCl_3.6H_2O$ were dissolved in 50 mL of DI water while being continuously stirred for 20 min at room temperature to obtain a uniform solution. Simultaneously, a KOH solution was prepared by dissolving a suitable quantity of KOH in 150 mL of DI water. The KOH solution was thoroughly stirred and heated to a temperature of 60 °C and maintained at 60 °C for 5 min. Gradually introduce the 50 mL solution containing $Zn(CH_3COO)_2.2H_2O$ and $YbCl_3.6H_2O$ into the KOH solution at a constant temperature of 60 °C. After adding all the 50 mL solutions, maintain the mixed solution at a temperature of 60 °C and vigorously stir for 60 min. Subsequently, the precipitated substance was filtered and washed by centrifugation using DI water and alcohol. The precipitated substance was then dried at 60 °C for 24 hours to yield $Zn_{1-x}Yb_xO$ nanocrystalline powder.

The $Zn_{1-x}Yb_xO$ nanoparticles were analyzed using powder X-ray diffraction (XRD) with CuKα radiation within the 2θ range of 20° to 80° and a scanning electron microscope (SEM). The FTIR spectroscopy was measured within the wavenumber range of 4000 to 400 cm^{-1}. The optical properties were evaluated by acquiring absorbance spectra using a UV-Vis spectrophotometer.

The evaluation of photocatalytic tests for the $Zn_{1-x}Yb_xO$ nanoparticles was conducted by observing RhB degradation. A solution of RhB with a concentration of 10 mg/L in a volume of 200 mL was mixed with 50 mg of the $Zn_{1-x}Yb_xO$ nanoparticles. The mixture was stirred in the absence of light for 30 min to achieve a state of equilibrium between the photocatalysts and RhB. Next, the mixture is exposed to radiation from a 250W mercury lamp. To determine the capacity for RhB decomposition, extract 4 mL of the solution at 5 min intervals and use centrifugation to eliminate the $Zn_{1-x}Yb_xO$ nanoparticles from the solution. The reduction in concentration of organic pollutants was tracked by recording their absorption signals. The percentage reduction is determined by applying the following formula:

$$DE = \frac{C_o - C_t}{C_o} x100\% \quad (1)$$

The initial concentration of RhB is denoted as "C_o", while the time-dependent concentration of RhB is denoted as "C_t".

RESULTS AND DISCUSSION

Surface mophology study

The surface morphology of the $Zn_{1-x}Yb_xO$ nanoparticles was examined using a SEM system as shown in Fig. 1. The $Zn_{1-x}Yb_xO$ nanoparticles sizes typically fall within the range of 30 to 50 nm and have a hexagonal nanoparticle morphology. However, $Zn_{0.93}Yb_{0.07}O$ nanoparticles lack a distinct hexagonal morphology. Previous studies also noted a similar finding in Gd- [21] and Ce-doped ZnO nanoparticles [22]. The primary factor contributing to the layered arrangement of doped ZnO nanoparticles is the presence of local forces, including Van der Waals forces, electric forces, chemical forces, and dipole-dipole forces, which are present throughout the synthesis process. These local forces contribute to hastening particle-particle interactions, resulting in the formation of agglomerates [23]

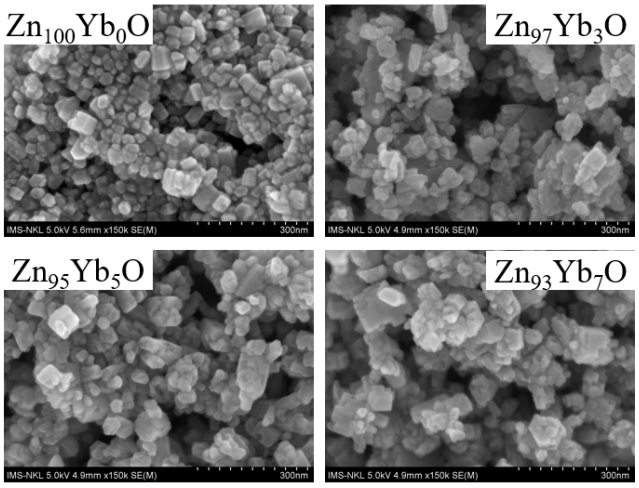

Figure 1. SEM images of the $Zn_{1-x}Yb_xO$ nanoparticles.

XRD analysis

Figure 2 illustrates the XRD pattern of the $Zn_{1-x}Yb_xO$ nanoparticles. When x = 0 (pure ZnO) diffraction peaks are observed at 31.77°, 34.44°, 36.25°, 47.49°, 56.57°, 62.85°, 66.35°, 67.94°, 69.08°, 72.62°, and 77.13° correspond to the lattice planes of (100), (002), (101), (102), (110), (103), (200), (112), (201), (004), and (202) represent the wurtzite hexagonal structure. The well-defined diffraction peaks confirm the high crystallinity of pure ZnO. When Yb was introduced to ZnO, the diffraction peaks became broader and there was a slight shift in the peak position, indicating the successful incorporation of Yb dopants into the hexagonal wurtzite structure, leading to a decrease in crystallinity. The peak broadening and shifting may be due to distortions in the ZnO crystal lattice due to the presence of Yb impurities. However, when the Yb content increased, no strange peaks appeared on the XRD diagram. This indicated that Yb does not form Yb_2O_3 but participates in the lattice cell of ZnO in a substitution or interstitial form.[24]

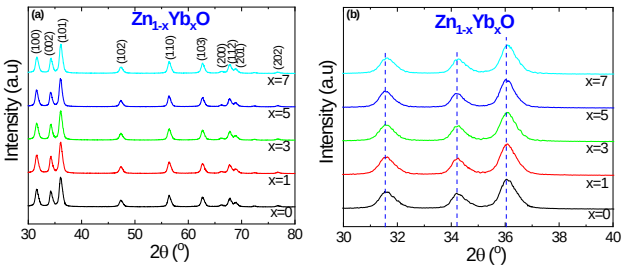

Figure 2. XRD patterns of the $Zn_{1-x}Yb_xO$ nanoparticles.

The Halder-Wagner technique [25] was used to determine the average size of the crystals and the strain in the crystal lattice of the nanostructures under investigation.

$$\left(\frac{\beta^*}{d^*}\right)^2 = \frac{1}{D}\frac{\beta^*}{d^2} + \left(\frac{\varepsilon}{2}\right)^2 \quad (2)$$

$$\beta^* = \frac{\beta.cos\theta}{\lambda} \quad (3)$$

$$d^* = \frac{2.sin\theta}{\lambda} \quad (4)$$

where λ is the wavelength of X-ray radiation, θ is the diffraction angle, and β is Full Width at Half Maximum. If the Lorentzian and Gaussian components of the function β^* represent the average crystal size and strain, respectively, then the function may be mathematically stated as:

$$\left(\frac{\beta}{tan\theta}\right)^2 = \frac{\kappa.\lambda}{D}\left(\frac{\beta}{tan\theta.sin\theta}\right) + \left(\frac{\varepsilon}{2}\right)^2 \quad (5)$$

$$\delta = \frac{1}{D^2} \quad (6)$$

The constant κ in this equation has a value of 4/3 [25]. Fig. 3 allows for the determination of the average crystal size and lattice strain by analyzing the relationship between: $\left(\frac{\beta}{tan\theta}\right)^2$ vs. $\left(\frac{\beta}{tan\theta.sin\theta}\right)$.

The average crystallite size of $Zn_{1-x}Yb_xO$ nanoparticles is determined to be 38.2 nm, 41.4 nm, 48.1 nm, 55.8 nm, and 60.7 nm, corresponding to the compositions of 0%, 1%, 3%, 5%, and 7% Yb, respectively. The presence of higher Yb impurity results in a larger crystal grain size and a lower dislocation density (δ), as measured by equation (6). Moreover, with the increase in Yb impurity, there is a definite observable increase in the intercept from $4.7x10^{-5}$ to $8.4x10^{-5}$, resulting in an increase in microscopic strain (ε). Tension strain is generated by positive values of microscopic strain. The findings obtained demonstrate a distinct distortion of the crystal lattice or an enlargement in the grain size of the $Zn_{1-x}Yb_xO$ nanoparticles when the Yb impurity is increased. The correlation between the Yb concentration and tensile strain and the increase in crystal size can be explained by the disparity in diameter between Yb (176 pm) and Zn (134 pm).

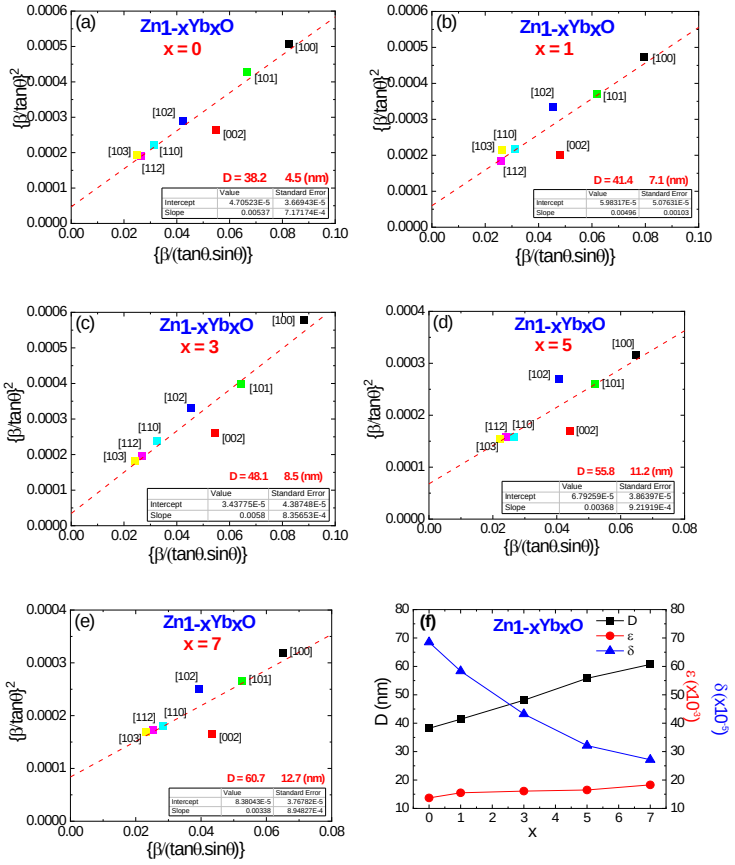

Figure 3. (a-e) Halder-Wagner plots of the seven most intense diffraction reflections for the $Zn_{1-x}Yb_xO$ nanoparticles, and (f) the average crystallite size, effective strain, and dislocation density of the $Zn_{1-x}Yb_xO$ nanoparticles.

FTIR analysis

The composition of the $Zn_{1-x}Yb_xO$ nanoparticles (0, 0.5, 1, 3, 5, 7, and 10 at.%) was evaluated by analyzing FTIR spectra spanning from 4000 cm^{-1} to 400 cm^{-1}, as shown in Fig. 4. Absorption bands were detected at the following wavenumbers: 3424, 2977, 2916, 1637, 1562, 1405, 1344, 1056, 902, and 567 cm^{-1}. The bands at around 3424 cm^{-1} and 1637 cm^{-1} are associated with the stretching vibrations of the hydroxyl group (-OH) and the carbonyl group (C=O), respectively [26]. Significantly, the -OH bands of ZnO nanoparticles have reduced intensity, which suggests the strength of the binding bands. The bands at 1562 cm^{-1} and 567 cm^{-1} were attributed to the stretching modes of Zn-O in the ZnO lattice [27]. The band seen at 2977 cm^{-1} and 2916 cm^{-1} may be attributed to the vibrations of CO_2 molecules that have been adsorbed on the surface of the $Zn_{1-x}Yb_xO$ nanoparticles [28]. The absorption peak at around 1405 cm^{-1} corresponds to the stretching vibration of the carbon-carbon double bond (C=C). The band associated with the C–O stretching vibration is observed at a wavelength of 1344 cm^{-1}, indicating the presence of secondary alcohol groups. The band at about 1056 cm^{-1} may be ascribed to the stretching mode of the aromatic C = C bond [29]. The absorption band corresponding to the stretching vibration of C–C bonds is observed at around 902 cm^{-1} [30]. Significantly, the intensity of the Zn−O band exhibited a

reduction after Yb doping. The drop in the intensity of the Zn−O band may be attributed to the integration of Yb ions into the crystal structure of ZnO, a finding confirmed by XRD examination.

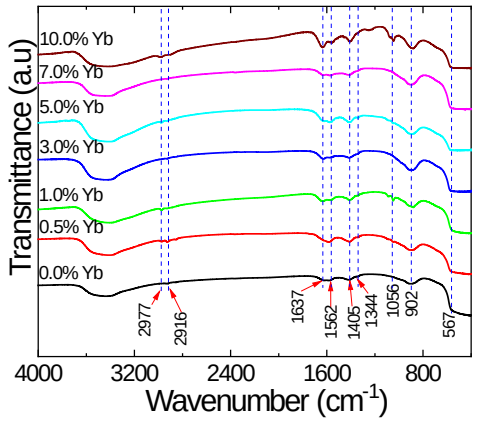

Figure 4. Fourier transform infrared (FTIR) spectra of the $Zn_{1-x}Yb_xO$ nanoparticles.

UV-Visible Absorption analysis

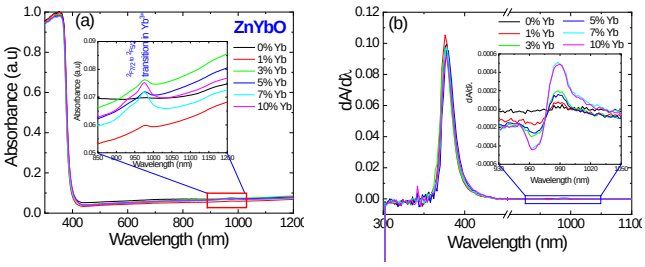

Figure 5. (a) The UV-visible absorption spectra of the $Zn_{1-x}Yb_xO$ nanoparticles. (b) The first derivative of the absorbance with respect to the photon wavelength.

The UV-Vis spectroscopy was employed to analyze the optical absorption spectrum of the $Zn_{1-x}Yb_xO$ nanoparticles, as depicted in Fig.5 (a). The $Zn_{1-x}Yb_xO$ nanoparticles exhibit a distinct absorption band at the wavelength of 378 nm, and a slight absorption shift is observed with variations in Yb impurity concentration. However, in the wavelength region shorter than 378 nm, a slight decrease in absorbance is noted for Yb-doped nanoparticles compared to pure ZnO nanoparticles. Additionally, noteworthy absorption peaks at a wavelength of 980 nm become evident when the Yb impurity ratio exceeds 1%. These peaks can be attributed to Yb absorption, specifically corresponding to the transition from the $^2F_{7/2}$ state to the $^2F_{5/2}$ state.[31] The determination of the band gap of the $Zn_{1-x}Yb_xO$ nanoparticles was calculated as the first derivative of absorbance with respect to wavelength (λ), as illustrated in Fig.5(b). The optical bandgap of the $Zn_{1-x}Yb_xO$ nanoparticles was established by studying the characteristic peaks at a wavelength of 378 nm. The results indicate that Yb integrates into the crystal lattice of ZnO, acting as photosensitive centers with a discrete transition at 980 nm. When Yb^{3+} replaces the position of Zn^{2+}, it not only enhances the carrier concentration in the $Zn_{1-x}Yb_xO$ nanoparticles but also contributes to expanding the optical absorption ability, especially in the near-infrared region. This characteristic makes the $Zn_{1-x}Yb_xO$ nanoparticles highly suitable for use as a photocatalyst.[19]

Magnetic analysis

Figure 6 depicts the magnetization against applied magnetic field (M(H)) data for the $Zn_{1-x}Yb_xO$ nanoparticles. The measurements were taken at room temperature and covered a range of magnetic fields from -5000 Oe to +5000 Oe. The findings of the magnetization characteristic measurement indicate substantial alterations in the magnetic characteristics of Yb-doped ZnO in comparison to undoped ZnO. Fig. 6 displays the magnetization curve of undoped ZnO, which has a negative slope. This indicates that the sample possesses diamagnetic properties when the applied magnetic field intensity exceeds 1200 Oe. Undoped ZnO displays modest ferromagnetism when the applied magnetic field falls within the range of -1200 Oe to +1200 Oe. The earlier work demonstrated the presence of ferromagnetism in undoped ZnO, which was found to be associated with inherent oxygen defects in ZnO [32,33]. The diamagnetic nature of ZnO is intrinsically linked to the filled 4d orbitals, namely the 3d10 electronic configuration of Zn^{2+} ions within ZnO. Therefore, ZnO, due to the absence of unpaired electrons in its d orbitals, will display either paramagnetic or ferromagnetic characteristics. Ferromagnetic characteristics are observed in Yb-doped ZnO samples when the contents of impurity exceed 5%. The saturation magnetization (M_S), remanent magnetization (M_R), and coercivity (H_C) values exhibit a positive correlation with the Yb impurity concentration in ZnO. The ferromagnetic feature of Yb-doped ZnO arises from the exchange interaction between Yb^{3+} ions and defect states in ZnO. The origin of ferromagnetism in Yb^{3+}-doped ZnO has been previously attributed to the bound magnetic polaron model (BMP) as described in earlier works.[32–35]

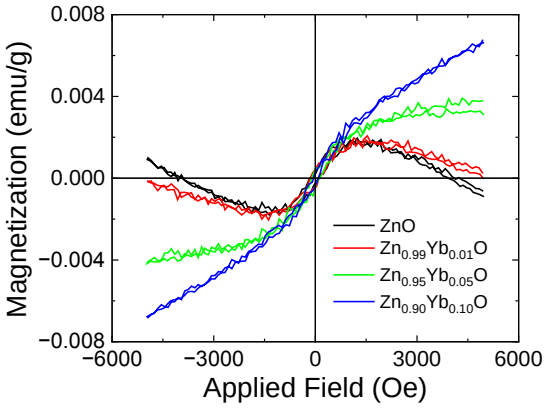

Figure 6. Room-temperature M(H) data of the $Zn_{1-x}Yb_xO$ nanoparticles.

Photocatalytic activities

An investigation was conducted to assess the photocatalytic efficiency of the $Zn_{1-x}Yb_xO$ nanoparticles in degrading Rhodamine B (RhB), which acts as a representative pollutant. The RhB intensity at a wavelength of 554 nm in Fig.7(a) exhibits a gradual decline over time, which corresponds to the photocatalytic

decomposition of the $Zn_{0.95}Yb_{0.05}O$ nanoparticles. Fig.7(b) demonstrates that the degradation rate of RhB by the $Zn_{1-x}Yb_xO$ nanoparticles through photocatalysis is influenced by the Yb doping concentration. Nevertheless, all samples exhibit a decomposition efficiency that can reach a maximum of 100% when the reaction time is 30 min. Through this fabrication technique, the ZnO material exhibits exceptional photocatalytic efficiency in comparison to previously reported findings, as demonstrated in Table 1. The photocatalytic activity is contingent upon the concentration of the phase. The complexity of the phenomenon can be ascribed to the efficacy of the Yb photosensitive centers. Furthermore, the photocatalytic degradation rate decreased with a higher doping concentration, potentially because the ZnO surface was shielded because of the increased Yb doping concentration.[36]

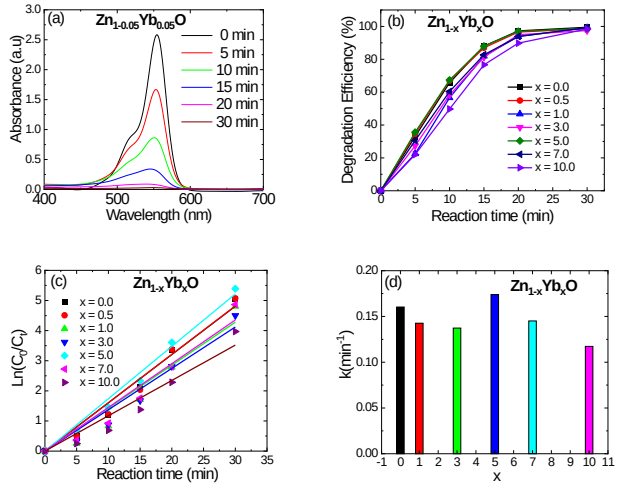

Figure 7. (a) The time-dependent UV–visible absorption spectra of RhB in the presence of the $Zn_{0.95}Yb_{0.05}O$ (x = 0.05) nanoparticles, (b) Photodegradation of RhB under Mercury lamp by the $Zn_{1-x}Yb_xO$ nanoparticles, (c) the first-order kinetic plot for RhB photodegradation, and (d) pseudo-order rate constant.

The photocatalytic activity of ZnO nanoparticles has been demonstrated to be strongly influenced by their size, with smaller nanoparticles providing higher photocatalytic activity [37]. The size of the nanoparticles in the $Zn_{1-x}Yb_xO$ nanoparticles exhibited an increase proportionate to the concentration of Yb doping. Thus, in principle, the degradation efficiency will rise proportionally with the increase in doping concentration. Unexpectedly, the highest degree of degradation occurs when using the $Zn_{0.95}Yb_{0.05}O$ nanoparticles (x = 0.05). This can be attributed to the response of the photosensitive centers Yb in the $Zn_{0.95}Yb_{0.05}O$ nanoparticles. This gives rise to the assumption that size may not be the primary determinant affecting the alteration in photocatalytic activity. A similar result regarding Ce-doped ZnO nanoparticles was found [38]. The report demonstrated that the concentration of Ce impurity has a significant impact on improving the photocatalytic properties of the ZnO nanoparticles.

To comprehend the influence of Yb doping on the photocatalytic efficacy of ZnO nanoparticles, it is imperative to understand the photocatalytic mechanisms in semiconductor materials. Experimental evidence clearly demonstrates that when irradiated to light with energies that are equal to or greater than the band gap, electrons in the valence band (VB) can transition to the conduction band (CB), resulting in the formation of holes in the VB. If there is a continuous separation of charges and dispersion of catalyst in RhB, both holes and electrons can move toward the surface of the particle. This migration contributes to redox reactions with the degradation of organic matter. This process is essential for photocatalytic activity. The assumption is that the variation in photocatalytic activity observed in the results is linked to the characteristics of the doping elements and their concentration in the $Zn_{1-x}Yb_xO$ nanoparticles.

The degradation kinetics of RhB were quantitatively analyzed to ascertain the rate constant. The degradation kinetics of RhB were observed to conform to pseudo-first-order kinetics:

$$ln\left(\frac{C_o}{C_t}\right) = kt$$

where C_o and C_t denote the initial and time-dependent concentration of RhB, t represents the time in min, and k is the rate constant in min^{-1}. According to the data shown in Fig.7(d), the rate constant of 5% Yb-doped ZnO is the highest among all the samples, while the 10% Yb-doped ZnO has the lowest rate constant, which represents the rate of RhB decomposition.

Figure 8 depicts the charge transfer mechanism in the $Zn_{1-x}Yb_xO$ nanoparticles. When Yb is incorporated into the crystal structure of ZnO, it generates energy levels within the bandgap of ZnO, resulting in the formation of additional energy levels for photosensitive centers. When the $Zn_{1-x}Yb_xO$ nanoparticles are illuminated, electron-hole pairs ($e^- - h^+$) are generated in its CB and VB, respectively. Electrons are involved in the process of reducing molecular oxygen to generate $*O_2^-$ in the CB. At the same time, the holes in VB interact with -OH to generate *OH radicals, which contribute to the reduction and decomposition of RhB.

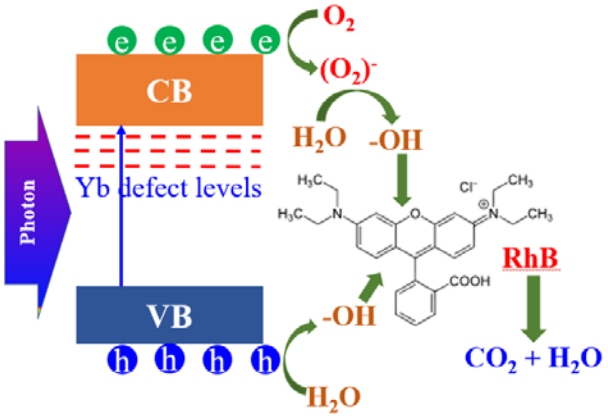

Fig.8. Schematic illustration of photocatalytic activity of the $Zn_{1-x}Yb_xO$ nanoparticles for the degradation of RhB.

Photocatalyst	Light soure/ Power	Type of dye	Photocatalyst dose (C_o)	Deg. (%)	Time (min)	Ref.
(Ag,Ce) co-doped ZnO	Xenon/300 W	RhB	30 mg/120 mL (10 ppm)	97	30	[20]
S doped ZnO	Xenon/ 1000 W/m^2	RhB	Film/100 mL (10 ppm)	92	150	39
Co doped ZnO	Sunlight/-	RhB	10 mg/100 mL (10 ppm)	81.22	120	40
		MB		86.98	90	
N-doped ZnO	UV/-	RhB	-	88	360	41
Ce doped ZnO	Solar light/-	MB	5 mg/5 mL (10 µM)	96.6	16	22
		RhB		77.7	16	
Ba doped ZnO	Visible light lamp/500 W	RhB	40 mg/100 mL (4.11 mg.L^{-1})	98.4	68	42
Er doped ZnO	Sun light/ 900 W/m^2	MB	5 mg/5 Ml (10 µM)	93.2	32	13
		MO		69.7	32	
(Er,Yb) co doped ZnO	Mercury Lamp/200 W	MO	25 mg/50 Ml (15 ppm)	98	90	19
$Zn_{0.95}Yb_{0.5}O$	Mercury lamp/250 W	RhB	50 mg/(200 mL) 10 ppm	97.3	20	This work

Table 1. Comparison of the photodegradation efficiency and rate of doped ZnO photocatalysts with this study.

CONCLUSION

The surface morphology of the $Zn_{1-x}Yb_xO$ nanoparticles, which typically range in size from 30 to 50 nm, is characterized by a hexagonal structure. The high crystallinity of the $Zn_{1-x}Yb_xO$ nanoparticles was confirmed by XRD. When Yb was introduced into ZnO, the diffraction peaks became broader and slightly shifted, indicating the successful incorporation of the Yb dopant into the hexagonal wurtzite structure of ZnO. The absorption bands of the $Zn_{1-x}Yb_xO$ nanoparticles are at 378 nm and transition peak of Yb can be observed at 980 nm, showing that Yb integrated into the ZnO crystal lattice, acting as photosensitive centers. The highest rate constant of RhB decomposition was obtained for the $Zn_{0.95}Yb_{0.05}O$ nanoparticles. Therefore, the $Zn_{1-x}Yb_xO$ nanoparticles can be effectively produced using the low temperature assisted co-precipitation method. The fabrication method exhibits high efficiency due to the presence of particles with uniform size, absence of any secondary phase, and exceptional photocatalytic performance. The results offer valuable insights into the selection of efficient fabrication techniques and doping elements to improve the photocatalytic properties of ZnO nanomaterials.

CONFLICT OF INTEREST STATEMENT

Authors declare that thể í no conflic of interest regarding the publication of this paper.

REFERENCES AND NOTES

1. A. Chauhan, G. Rana, V. Dutta, et al. Recent trends in phyto-mediated iron-based nanomaterials for environmental remediation and biomedical applications. *Inorganic Chemistry Communications* **2024**, 160, 111976.
2. R. Mahadevan, S. Palanisamy, P. Sakthivel. Role of nanoparticles as oxidation catalyst in the treatment of textile wastewater: Fundamentals and recent advances. *Sustainable Chemistry for the Environment* **2023**, 4, 100044.
3. R.O. Ocaya, Y. Orman, A.G. Al-Sehemi, et al. Bias and illumination-dependent room temperature negative differential conductance in Ni-doped ZnO/p-Si Schottky photodiodes for quantum optics applications. *Heliyon* **2023**, 9 (5), e16269.
4. C. Klingshirn, J. Fallert, O. Gogolin, et al. Linear and nonlinear optics, dynamics, and lasing in ZnO bulk and nanostructures. *Journal of Luminescence* **2008**, 128 (5–6), 792–796.
5. S. Sardar, P. Kar, S.K. Pal. The Impact of Central Metal Ions in Porphyrin Functionalized ZnO/TiO2 for Enhanced Solar Energy Conversion. *J. Mater. Nanosci.* **2014**, 1 (1), 12–30..
6. T. Yang, H. Pan, G. Tian, et al. Hierarchically structured PVDF/ZnO core-shell nanofibers for self-powered physiological monitoring electronics. *Nano Energy* **2020**, 72, 104706.
7. P. Supraja, R.R. Kumar, S. Mishra, et al. A simple and low-cost triboelectric nanogenerator based on two dimensional ZnO nanosheets and its application in portable electronics. *Sensors and Actuators A: Physical* **2022**, 335, 113368.
8. A. Al-Rasheedi, A. Salwati, A.R. Ansari, A.A.-D. Hassaneen, M.S. Aida. Photocatalysis activity of ZnO nanorods arrays prepared via hydrothermal. *Inorganic Chemistry Communications* **2023**, 158, 111568.
9. L.Z. Fogaça, J.C.M. Vicentini, C.F. De Freitas, et al. Nanocomposites of Nb2O5 and ZnO with reduced graphene oxide for heterogeneous photocatalysis of dyes. *Catalysis Communications* **2023**, 185, 106799.
10. A. Ashpak Shaikh, M. Rajendra Patil, B. Sonu Jagdale, V. Ashok Adole. Synthesis and characterization of Ag doped ZnO nanomaterial as an effective photocatalyst for photocatalytic degradation of Eriochrome Black T dye and antimicrobial agent. *Inorganic Chemistry Communications* **2023**, 151, 110570.
11. S.S.A. Al Ghafry, H. Al Shidhani, B. Al Farsi, et al. The photocatalytic degradation of phenol under solar irradiation using microwave-assisted Ag-doped ZnO nanostructures. *Optical Materials* **2023**, 135, 113272.
12. X. Wang. The Comparison of Titanium Dioxide and Zinc Oxide Used in Sunscreen Based on Their Enhanced Absorption. *ACE* **2023**, 24 (1), 237–245.
13. S. Choudhary, S. Mohapatra. Enhanced photocatalytic activity of Er doped ZnO nanospindles and nanorods for degradation of organic pollutants. *Inorganic Chemistry Communications* **2024**, 161, 111977.
14. S. Karakaya, L. Kaba. Wrinkle type nanostructured of Al-Ce co-doped ZnO thin films for photocatalytic applications. *Surfaces and Interfaces* **2024**, 44, 103655.
15. A.S. Rini, A.P. Defti, R. Dewi, Jasril, Y. Rati. Biosynthesis of nanoflower Ag-doped ZnO and its application as photocatalyst for Methylene blue degradation. *Materials Today: Proceedings* **2023**, 87, 234–239.

16. L. Hao, M. Adnan Kamboh, Y. Su, et al. First-principles study of electronic states, optical properties, water adsorption and dissociation properties of Pt-doped two-dimensional ZnO. *Materials Science and Engineering: B* **2022**, 286, 116019.
17. M. Faisal, J. Ahmed, J.S. Algethami, et al. Au nanoparticles dispersed chitosan/ZnO ternary nanocomposite as a highly efficient and reusable visible light photocatalyst. *Materials Science in Semiconductor Processing* **2023**, 167, 107798.
18. C.J. Bueno-Alejo, J. Graus, R. Arenal, et al. Anisotropic Au-ZnO photocatalyst for the visible-light expanded oxidation of n-hexane. *Catalysis Today* **2021**, 362, 97–103.
19. I. Ahmad. Inexpensive and quick photocatalytic activity of rare earth (Er, Yb) co-doped ZnO nanoparticles for degradation of methyl orange dye. *Separation and Purification Technology* **2019**, 227, 115726.
20. R. Liu, X. Fu, Y. Guo, J. Zhang, W. Tian. A study on Ag or Ce doped and co-doped ZnO for the photocatalytic degradation of RhB dye. *Vacuum* **2023**, 215, 112337.
21. M. Isik, N.M. Gasanly. Gd-doped ZnO nanoparticles: Synthesis, structural and thermoluminescence properties. *Journal of Luminescence* **2019**, 207, 220–225.
22. S. Choudhary, M. Sharma, V. Krishnan, S. Mohapatra. Facile synthesis of Ce doped ZnO nanowires for efficient photocatalytic removal of organic pollutants from water. *Materials Today Communications* **2023**, 34, 105361.
23. M. Isik, N.M. Gasanly. The defect state of Yb-doped ZnO nanoparticles using thermoluminescence study. *Materials Science in Semiconductor Processing* **2019**, 100, 29–34.
24. D.E. Navarro-López, R. Garcia-Varela, O. Ceballos-Sanchez, et al. Effective antimicrobial activity of ZnO and Yb-doped ZnO nanoparticles against Staphylococcus aureus and Escherichia coli. *Materials Science and Engineering: C* **2021**, 123, 112004.
25. S.A. Disha, Md. Sahadat Hossain, Md.L. Habib, S. Ahmed. Calculation of crystallite sizes of pure and metals doped hydroxyapatite engaging Scherrer method, Halder-Wagner method, Williamson-Hall model, and size-strain plot. *Results in Materials* **2024**, 21, 100496.
26. M.N. Siddique, T. Ali, A. Ahmed, P. Tripathi. Enhanced electrical and thermal properties of pure and Ni substituted ZnO Nanoparticles. *Nano-Structures & Nano-Objects* **2018**, 16, 156–166.
27. M.L. Da Silva-Neto, M.C.A. De Oliveira, C.T. Dominguez, et al. UV random laser emission from flexible ZnO-Ag-enriched electrospun cellulose acetate fiber matrix. *Sci Rep* **2019**, 9 (1), 11765.
28. G. Nagaraju, Udayabhanu, Shivaraj, et al. Electrochemical heavy metal detection, photocatalytic, photoluminescence, biodiesel production and antibacterial activities of Ag–ZnO nanomaterial. *Materials Research Bulletin* **2017**, 94, 54–63.
29. O.M. Ntwaeaborwa, S.J. Mofokeng, V. Kumar, R.E. Kroon. Structural, optical and photoluminescence properties of Eu 3+ doped ZnO nanoparticles. *Spectrochimica Acta Part A: Molecular and Biomolecular Spectroscopy* **2017**, 182, 42–49.
30. M. Arshad, A. Azam, A.S. Ahmed, S. Mollah, A.H. Naqvi. Effect of Co substitution on the structural and optical properties of ZnO nanoparticles synthesized by sol–gel route. *Journal of Alloys and Compounds* **2011**, 509 (33), 8378–8381.
31. N.T. Dung, H.V. Thanh, N.D. Lam. Influences of Growth Durations on Characteristics of NaYF4:(Yb,Tm) Upconversion Materials. *NST* **2019**, 35 (4).
32. C. Guglieri, E. Céspedes, A. Espinosa, et al. Evidence of Oxygen Ferromagnetism in ZnO Based Materials. *Adv Funct Materials* **2014**, 24 (14), 2094–2100.
33. N. Bhakta, T. Inamori, R. Shirakami, et al. Room temperature magnetic ordering and analysis by bound magnetic polaron model of Yb3+ doped nanocrystalline zinc oxide (Zn0.98Yb0.02O). *Materials Research Bulletin* **2018**, 104, 6–14.
34. Y. Tan, Z. Fang, W. Chen, P. He. Structural, optical and magnetic properties of Eu-doped ZnO films. *Journal of Alloys and Compounds* **2011**, 509 (21), 6321–6324.
35. Y. Jiang, W. Yan, Z. Sun, et al. Experimental and theoretical investigations on ferromagnetic nature of Mn-doped dilute magnetic semiconductors. *J. Phys.: Conf. Ser.* **2009**, 190, 012100.
36. R. Kumar, A. Umar, G. Kumar, et al. Ce-doped ZnO nanoparticles for efficient photocatalytic degradation of direct red-23 dye. *Ceramics International* **2015**, 41 (6), 7773–7782.
37. M.C. Uribe-López, M.C. Hidalgo-López, R. López-González, et al. Photocatalytic activity of ZnO nanoparticles and the role of the synthesis method on their physical and chemical properties. *Journal of Photochemistry and Photobiology A: Chemistry* **2021**, 404, 112866.
38. J. Lang, J. Wang, Q. Zhang, et al. Chemical precipitation synthesis and significant enhancement in photocatalytic activity of Ce-doped ZnO nanoparticles. *Ceramics International* **2016**, 42 (12), 14175–14181.
39. Y. Rati, Y.N. Hendri, R. Waluyo, et al. Visible light assisted degradation of Rhodamin B by reusable S-doped ZnO thin film photocatalyst. *Optical Materials* **2023**, 135, 113370.
40. L.H. Mohammed, F. Gulbagca, R.N.E. Tiri, et al. Hydrothermal-assisted synthesis of Co-doped ZnO nanoparticles catalyst for sodium borohydride dehydrogenation and photodegradation of organic pollutants in water. *Chemical Engineering Journal Advances* **2023**, 14, 100495.
41. S. Mondal, S.A. Ayon, M.S. Islam, M.S. Rana, M.M. Billah. Morphological evaluation and boosted photocatalytic activity of N-doped ZnO nanoparticles prepared via Co-precipitation method. *Heliyon* **2023**, 9 (10), e20948.
42. B. Shirdel, M.A. Behnajady. Visible-light-induced degradation of Rhodamine B by Ba doped ZnO nanoparticles. *Journal of Molecular Liquids* **2020**, 315, 113633.